

Solid redox equilibrium via d-band centers regulation in the MoS₂/Ni₃S₂ heterojunction for efficient selective oxidation of 5-hydroxymethylfurfural

Yiqing Sun ^a, Yiwei Bao ^a, Xiuming Bu ^{a,*,**}, Kaihang Yue ^a, Hao Zhang ^a, Yuxuan Zhang ^b, Di Yin ^b, Siwei Yang ^c, Johnny C. Ho ^{b,*}, Xianying Wang ^{a,***}

^a CAS Key Laboratory of Materials for Energy Conversion, Shanghai Institute of Ceramics, Chinese Academy of Sciences (SICCAS), Shanghai 200050, PR China

^b Department of Materials Science and Engineering, City University of Hong Kong, Kowloon, Hong Kong SAR 999077, PR China

^c Joint Laboratory of Graphene Materials and Applications, State Key Laboratory of Functional Materials for Informatics, Shanghai Institute of Microsystem and Information Technology, Chinese Academy of Sciences, Shanghai 200050, PR China

ARTICLE INFO

Article history:

Received 30 October 2023

Received in revised form

21 November 2023

Accepted 21 November 2023

Available online 25 November 2023

Keywords:

Two-dimensional

Electrocatalyst

Heterostructure

5-Hydroxymethylfurfural

d-Band center

ABSTRACT

The 5-hydroxymethylfurfural electrocatalytic oxidation reaction (HMFOR), in coupling with the hydrogen evolution reaction (HER), can replace the kinetically slow anodic oxygen evolution reaction (OER) to produce high value oxides and hydrogen. However, the commonly employed Ni-based electrocatalyst exhibits an unsatisfied performance due to the existence of OER. Here, we design and synthesize the Ni₃S₂/MoS₂/NiMoO₄ catalyst for efficient and stable HMFOR reaction. Through the in situ Raman spectroscopy, we demonstrate that the Ni^{III}-OOH formed during the surface reconstruction process is the real reactive species for HMFOR. Moreover, the density functional theory results show that the upward shift of d-band centers in the reconstructed NiOOH/MoS₂ is beneficial for the HMF adsorption and guarantees the smooth progression of redox equilibrium reactions. As a result, the prepared electrocatalyst shows a good HMFOR electrocatalytic performance in terms of selectivity (99.2%), conversion (96.7%), and Faraday efficiency (96.5%).

© 2023 Elsevier Ltd. All rights reserved.

1. Introduction

Currently, the majority of the energy and chemicals that modern society rely on come from the conversion of fossil fuels, and the preparation and production processes have caused a serious energy crisis and environmental pollution [1–3]. The utilization of biomass through green technology provides a promising solution and a new direction for sustainable development [4,5]. Recently, 5-hydroxymethylfurfural (HMF), a biomass-derived molecule, has received considerable attention because its oxidation product, 2,5-furandicarboxylic acid (FDCA), serves as a common precursor in the production of poly(ethylene glycol) furfurylcarboxylate, which is recognized as a biopolymer and a valuable oxide in biopolymer

production. Compared to conventional thermochemical methods employed to synthesize FDCA (expensive precious metal catalysts, harsh working conditions, and unsatisfied yields), electrochemical oxidation methods driven by renewable energy sources have been demonstrated as a more promising solution for synthesizing FDCA [6–8]. Meanwhile, the electrooxidation potential of HMF (0.113 V) is significantly lower than that of the oxygen evolution reaction (OER, 1.23 V), suggesting that HMF electrocatalytic oxidation reaction (HMFOR) not only replaces the sluggish OER process at the anode, but also couples with the hydrogen evolution reaction process at the cathode to produce economically valuable hydrogen [9,10].

During the HMFOR process, the catalyst surface not only undergoes the aldehyde or hydroxyl oxidation process of HMF, but also experiences the in-situ surface reconstruction behavior driven by an external voltage [11,12]. Our research group has recently demonstrated, through the in-situ Raman technique, that the surface-reconstructed high-valent Ni^{III}-OOH species is the actual active site for HMFOR, which undergoes a redox reaction with the HMF, oxidizing the HMF while simultaneously being reduced to the

* Corresponding author.

** Corresponding author.

*** Corresponding author.

E-mail addresses: buxiuming@mail.sic.ac.cn (X. Bu), johnnyho@cityu.edu.hk (J.C. Ho), wangxianying@mail.sic.ac.cn (X. Wang).

low-valent Ni^{II} species [12]. However, it is worth noting that OER as a competitive reaction of HMFOR in the alkaline electrolyte, the enhancement of the OER reaction kinetics at high voltages will result in some part of the Ni^{III}-OOH species taking part in OER rather than HMFOR, breaking the dynamic redox equilibrium and reducing the utilization efficiency of the active species [6,13]. Therefore, it is still a challenge to solidify the redox equilibrium between the HMF and Ni^{III}-OOH species under a high potential to achieve the higher HMFOR catalytic activity.

In this work, we designed and synthesized Ni₃S₂/MoS₂/NiMoO₄ materials, two-dimensional (2D) Ni₃S₂/MoS₂ heterojunction nanosheets anchored on the surface of NiMoO₄ nano-arrays, as electrocatalysts for highly efficient HMFOR. By combining theoretical calculation and experimental characterization, we demonstrated that the upward shift of d-band centers in the reconstructed NiOOH/MoS₂ is beneficial for the HMF adsorption and guarantees the smooth progression of redox equilibrium reactions under a high potential. As a result, the fabricated catalyst showed superior catalytic performance, with a potential reduction of 233 mV for HMFOR at a current density of 100 mA/cm² compared to the OER

process, an FDCA selectivity of 96.7%, and a Faraday efficiency of 96.5%. Our work not only confirms the potential of Ni₃S₂/MoS₂/NiMoO₄ catalyst for practical applications, but also provides new insights for the design of high performance HMFOR catalysts.

2. Results and discussion

2.1. Characterization of electrocatalysts

For the synthesis of Ni₃S₂/MoS₂/NiMoO₄ electrocatalysts, NiMo precursors were first prepared hydrothermally on nickel foams (NF), followed by sulfidation at high temperatures in the Ar atmosphere (Fig. 1a, detailed preparation process was shown in the Experiment section). From the scanning electron microscopy (SEM) images in Fig. 1b and Figs. S1a–b, it can be seen that the pure NiMo precursor exhibits a nanorod-like structure (about 1 μm) with a smooth surface. After the high temperature sulfurization treatment, the otherwise smooth surface of the NiMoO₄ nanorods is uniformly and densely covered with 2D nanosheets (Fig. 1c). Atomic force microscopy and the corresponding height distribution map were used to

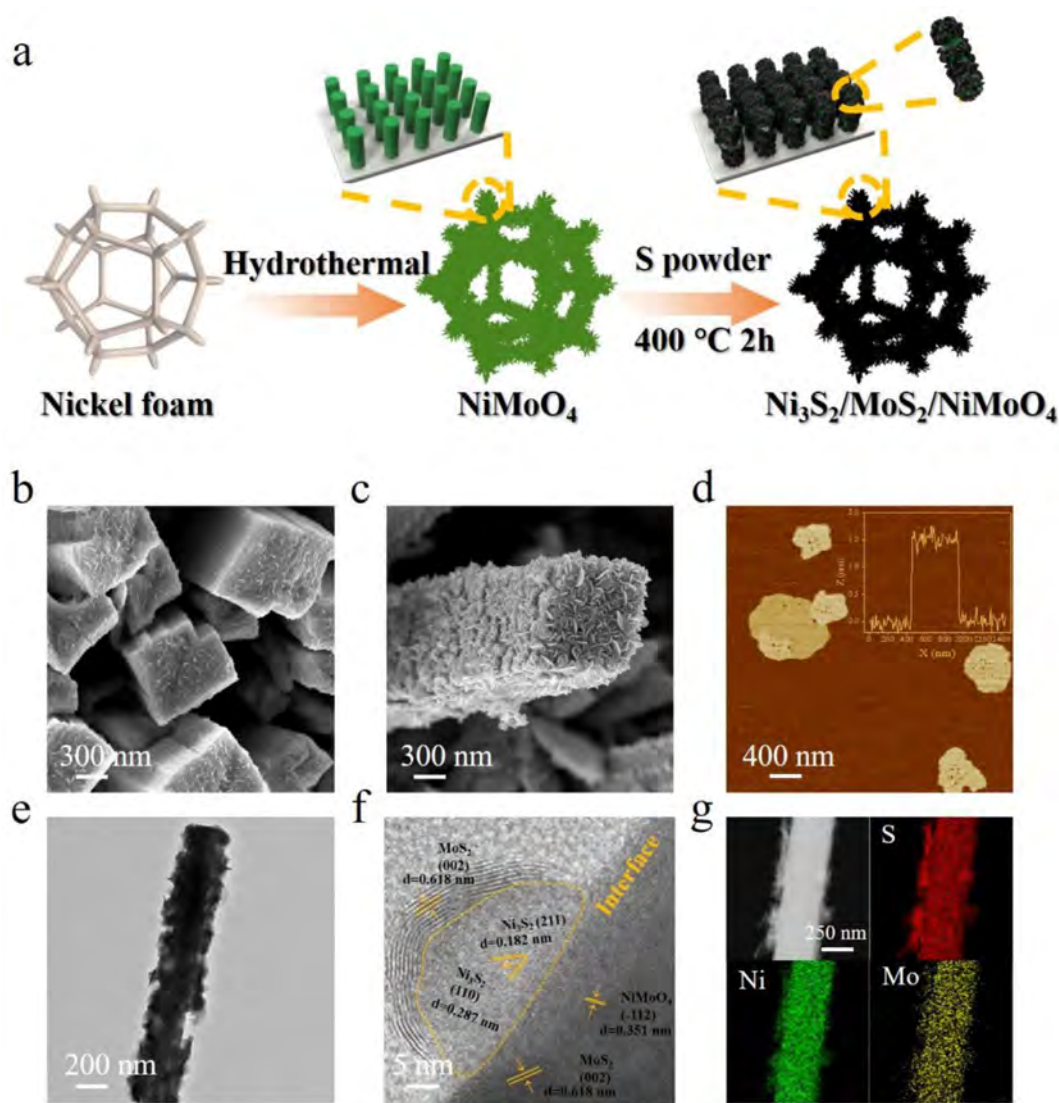


Fig. 1. (a) Schematic illustration of the synthesis of Ni₃S₂/MoS₂/NiMoO₄. (b) and (c) SEM images of NiMoO₄ and Ni₃S₂/MoS₂/NiMoO₄. (d) Atomic force microscopy (AFM) image of Ni₃S₂/MoS₂. (e) TEM and (f) High-resolution transmission electron microscopy (HRTEM) images of Ni₃S₂/MoS₂/NiMoO₄. (g) STEM image and corresponding energy dispersive spectroscopy (EDS) mapping of Ni₃S₂/MoS₂/NiMoO₄ for S, Ni, and Mo elements. AFM: atomic force microscopy; HRTEM: high-resolution transmission electron microscopy.

illustrate that the thickness of these 2D nanosheets is approximately 2 nm (Fig. 1d). In addition, the obtained N₂ adsorption/desorption isotherms further proved that the Brunauer–Emmett–Teller surface area of Ni₃S₂/MoS₂/NiMoO₄ (15.96 m²/g) is much larger than that of NiMoO₄ (4.73 m²/g) (Figs. S2 and S3). The in-situ formation of two-dimensional nanosheets on the nanorods increases the active sites exposed, which is favorable for a fast electron transport kinetic. Further detailed structural information is provided by high-resolution transmission electron microscopy, the characteristic lattice fringes measuring 0.182 and 0.287 nm correspond accurately with the (002) and (110) planes of Ni₃S₂. The angle between the two crystal faces (46°) further confirms this observation. In addition, the characteristic lattice fringes of 0.618 and 0.351 nm belong to the (002) plane of MoS₂ and (−110) plane of NiMoO₄, respectively (Figs. 1f and S4). Moreover, as shown in Fig. 1g, the energy dispersive X-ray elemental mapping collected under a high-angle annular dark-field scanning transmission electron microscope showed the presence of S, Mo, and Ni elements throughout NiMoO₄ and the uniform distribution of these elements. The above observations not only prove the successful formation of Ni₃S₂/MoS₂/NiMoO₄ electrocatalysts, but also demonstrate the close contact between Ni₃S₂ and MoS₂.

For additional information on the phase composition of Ni₃S₂/MoS₂/NiMoO₄, the X-ray diffraction (XRD) patterns for Ni₃S₂/MoS₂/NiMoO₄, NiMoO₄ and Ni₃S₂ samples are shown in Fig. 2a. In addition to the obvious peak of the NF, the characteristic peaks at 14.2°, 25.3°, 28.8°, and 32.8° correspond to the (110), (−112), (220), and (−321) crystal planes of NiMoO₄ (PDF No. 33-0948) [14]. Another four diffraction peaks at 21.7°, 31.1°, 49.7°, and 50.1° could be indexed to the (101), (110), (113), and (211) crystal planes of Ni₃S₂

(PDF No. 44-1418) [15]. Raman spectroscopy was used to determine the structure and composition of Ni₃S₂/MoS₂/NiMoO₄ (Fig. 2b). Strong characteristic peaks at 709, 907, and 957/cm are observed both on NiMoO₄ and Ni₃S₂/MoS₂/NiMoO₄. The peaks at 907 and 957/cm are assigned to the symmetric and asymmetric stretching modes of the Mo=O bond, while the peak at 709/cm belongs to the asymmetric modes of the Ni–Mo–O bond [16,17]. But after the sulfidation treatment, new Raman peaks at 200–350/cm, 375/cm and 405/cm appeared, which corresponds to the vibration mode of the Ni–S bond, A_{1g} mode and E_{12g} mode of the 2H phase of MoS₂ [18,19].

The surface electronic structure and chemical composition of the samples were further elucidated by X-ray photoelectron spectroscopy (XPS) (Figs. 2c–f, S5 and S6). The XPS survey spectrum confirms the presence of Ni, Mo, S, and O elements in Ni₃S₂/MoS₂/NiMoO₄ (Fig. 2c). The high-resolution Ni 2p spectrum of Ni₃S₂/MoS₂/NiMoO₄ (Fig. 2d) can be fitted into two spin-orbit doublet peaks, consisting of two peaks at 854.8 and 872.3 eV belonging to Ni²⁺ 2p_{3/2}, and 2p_{1/2} while another two peaks at 856.5 and 874.2 eV correspond to Ni³⁺ 2p_{3/2} and 2p_{1/2} [20]. Meanwhile, their corresponding satellite peaks can be observed at 862.0 and 879.8 eV, respectively [20]. Likewise, as for the high-resolution Mo 3d spectrum (Fig. 2e), besides the binding energy of 235.8 eV for Mo⁶⁺, another set of peaks at 229.1 and 232.5 eV are characteristic of Mo⁴⁺ in MoS₂ [18,21]. In addition, the single peak at the binding energy of 226.2 eV is attributed to the formation of Ni–S–Mo species due to S 2s. After the high temperature sulfidation, the high-resolution S 2p spectrum in Fig. 2f displays two peaks located at 161.8 and 163.0 eV, attributed to S 2p_{3/2} and 2p_{1/2}, which can be assigned to the S atoms bonded to Ni [22]. More importantly,

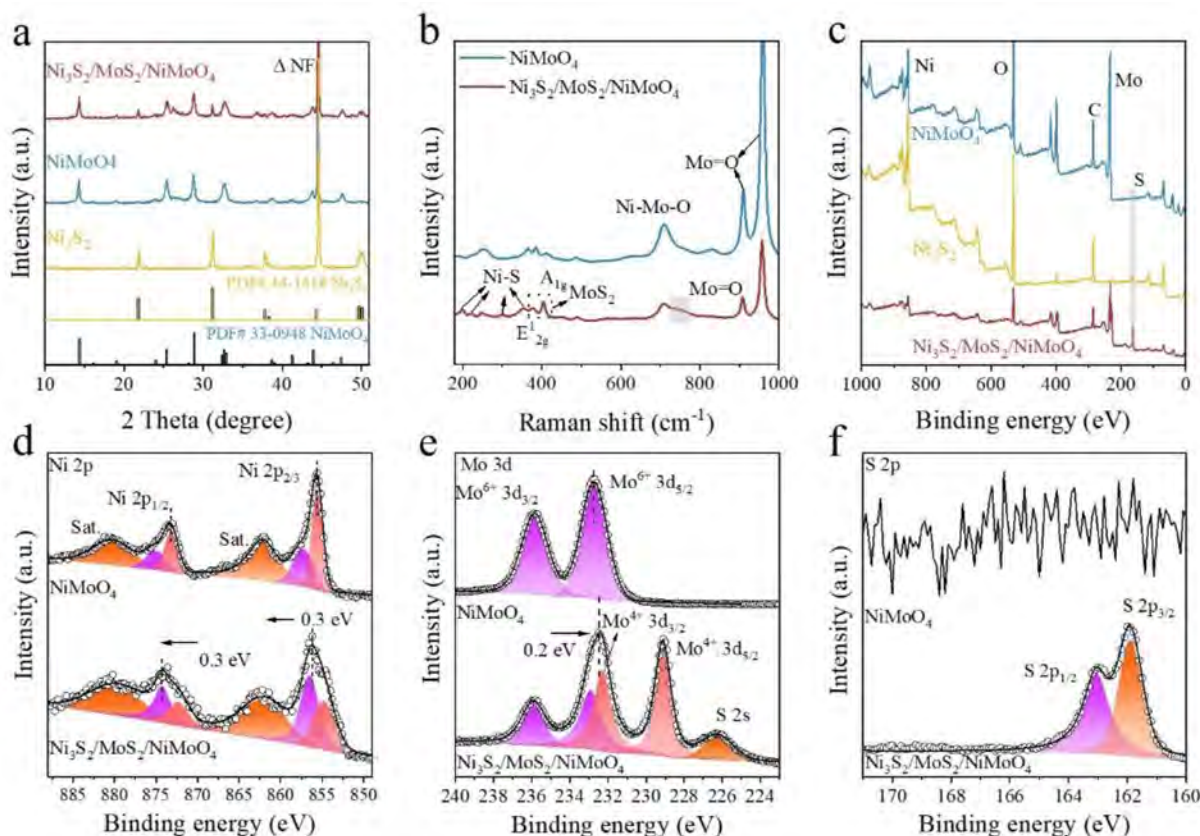


Fig. 2. (a) XRD patterns of Ni₃S₂/MoS₂/NiMoO₄, NiMoO₄ and Ni₃S₂. (b) Raman spectrum of Ni₃S₂/MoS₂/NiMoO₄ and NiMoO₄. (c) XPS spectra of the Ni₃S₂/MoS₂/NiMoO₄, NiMoO₄ and Ni₃S₂. (d) and (e) High-resolution XPS spectra of Ni 2p and Mo 3d for Ni₃S₂/MoS₂/NiMoO₄ and NiMoO₄. (f) High-resolution XPS spectra of S 2p for Ni₃S₂/MoS₂/NiMoO₄ and NiMoO₄.

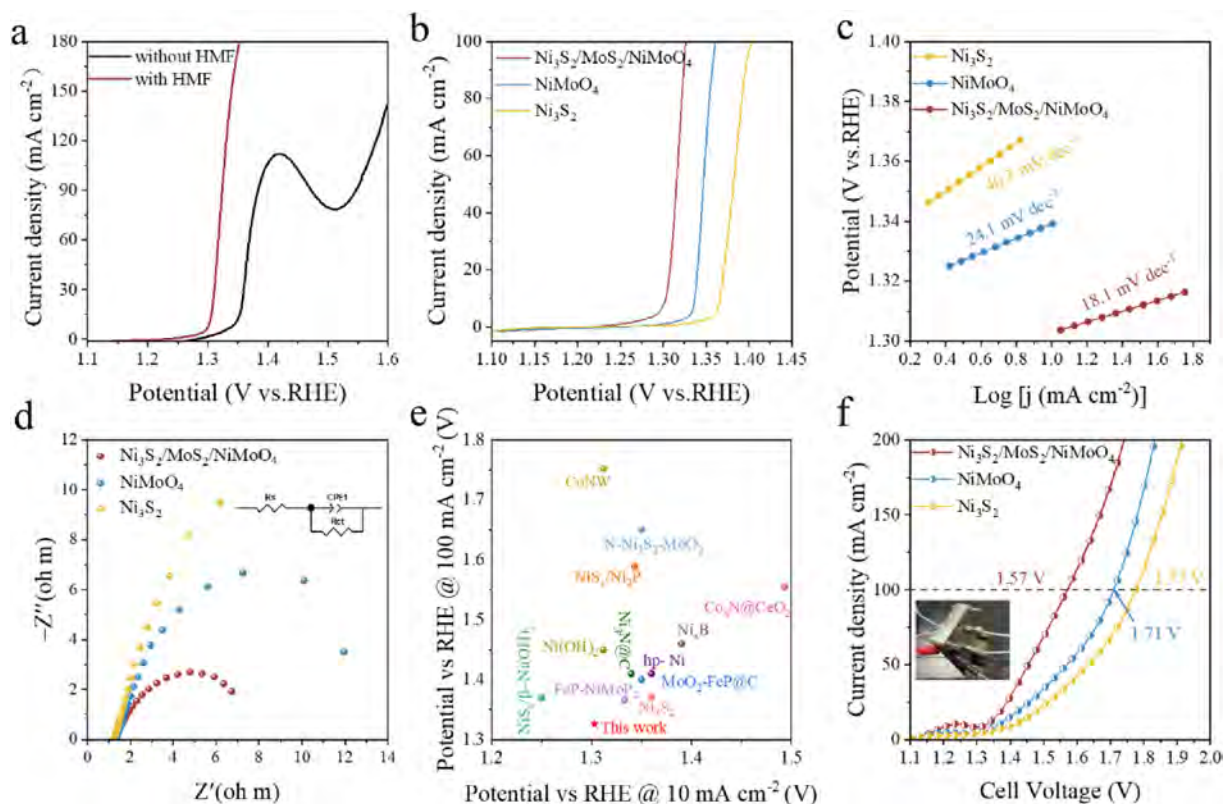


Fig. 3. (a) Polarization curves of $\text{Ni}_3\text{S}_2/\text{MoS}_2/\text{NiMoO}_4$ in 1.0 M KOH with and without 50 mM HMF. (b) Polarization of $\text{Ni}_3\text{S}_2/\text{MoS}_2/\text{NiMoO}_4$, NiMoO_4 , and Ni_3S_2 in 1.0 M KOH with 50 mM HMF. (c) Tafel slopes for different electrodes. (d) Nyquist plots. (e) Comparison of performance with other recently reported HMFOR electrocatalysts. (f) Polarization curves of the $\text{Ni}_3\text{S}_2/\text{MoS}_2/\text{NiMoO}_4$ (+) || NiFe LDH (-), NiMoO_4 (+) || NiFe LDH (-) and Ni_3S_2 (+) || NiFe LDH (-) assembled flow cells in 1.0 M KOH with 50 mM HMF.

compared with NiMoO_4 , the binding energy of Ni 2p in $\text{Ni}_3\text{S}_2/\text{MoS}_2/\text{NiMoO}_4$ is positively shifted by 0.3 eV, while the binding energy of Mo 3d is negatively shifted by 0.2 eV. These conclusions suggest that there is a redistribution of electrons between Ni_3S_2 and MoS_2 , leading to the electrons transferred from Ni_3S_2 to MoS_2 . Due to the existence of the close heterogeneous interface, the electronic cloud is rearranged, which is of great significance in regulating the catalytic performance.

2.2. Electrocatalytic performance of HMFOR

To shed light on the good electrocatalytic characteristics induced by the heterostructure establishment, the electrocatalytic HMFOR performance of the evaluation of $\text{Ni}_3\text{S}_2/\text{MoS}_2/\text{NiMoO}_4$ is by means of a typical three-electrode system. As demonstrated by linear sweep voltammetry (LSV) in Fig. 3a, the $\text{Ni}_3\text{S}_2/\text{MoS}_2/\text{NiMoO}_4$ electrode exhibited obvious current response when 50 mM HMF was added into the 1.0 M KOH electrolyte. Significantly, the current density of $100 \text{ mA}/\text{cm}^2$ is achieved at only 1.326 V (vs. RHE), which is 233 mV lower than that of the OER, suggesting the high value-added by-product are harvested and consumption is reduced. In addition, the obvious anodic peak located near 1.45 V suggests the transformation from Ni^{II} species to Ni^{III} species, indicating the surface reconstruction process occurs on the electrode surface [12,23,24]. Subsequently, compared with NiMoO_4 and Ni_3S_2 , the $\text{Ni}_3\text{S}_2/\text{MoS}_2/\text{NiMoO}_4$ has the lower onset potential and the higher oxidation current density (Fig. 3b), which proves that $\text{Ni}_3\text{S}_2/\text{MoS}_2/\text{NiMoO}_4$ catalyst has good HMFOR performance. The corresponding Tafel slope of $\text{Ni}_3\text{S}_2/\text{MoS}_2/\text{NiMoO}_4$ was calculated to be 18.1 mV/dec, which is smaller than that

of NiMoO_4 (24.1 mV/dec) and Ni_3S_2 (40.3 mV/dec), indicating that the $\text{Ni}_3\text{S}_2/\text{MoS}_2/\text{NiMoO}_4$ catalyst has the fastest HMFOR reaction kinetics (Fig. 3c). Additionally, the Nyquist plot of $\text{Ni}_3\text{S}_2/\text{MoS}_2/\text{NiMoO}_4$ shows a semicircle with the smallest diameter, and the construction of an equivalent circuit diagram demonstrates that the charge transfer resistance (R_{ct}) of $\text{Ni}_3\text{S}_2/\text{MoS}_2/\text{NiMoO}_4$ is as low as 2.479Ω (Fig. 3d), which indicates that the formation of heterogeneous structures can accelerate surface charge transfer. In addition, cyclic voltammetry (CV) is used to measure the non-Faraday electrochemical double layer capacitance (C_{dl}) of $\text{Ni}_3\text{S}_2/\text{MoS}_2/\text{NiMoO}_4$, NiMoO_4 and Ni_3S_2 at different scans from 50 mV/s to 250 mV/s to estimate their electrochemical active surface area (Fig. S7). As shown in Fig. S7, the current densities in CV curves of $\text{Ni}_3\text{S}_2/\text{MoS}_2/\text{NiMoO}_4$ are much higher than those of NiMoO_4 and Ni_3S_2 . $\text{Ni}_3\text{S}_2/\text{MoS}_2/\text{NiMoO}_4$ also has the largest C_{dl} value of $8.6 \text{ mF}/\text{cm}^2$, which reveals that the unique 2D nanostructure formed after the sulfidation treatment exposes more active sites, so that the $\text{Ni}_3\text{S}_2/\text{MoS}_2/\text{NiMoO}_4$ can better capture HMF molecules and improve catalytic performance. Compared with the most advanced HMFOR electrocatalysts, the HMFOR activity of $\text{Ni}_3\text{S}_2/\text{MoS}_2/\text{NiMoO}_4$ is almost the best reported so far (Fig. 3e and Table S1).

Moreover, considering the high HMFOR performance, we assembled the prepared electrodes with homemade NiFe LDH catalysts in an anion-exchange membrane water electrolyzer to further investigate the practical application of $\text{Ni}_3\text{S}_2/\text{MoS}_2/\text{NiMoO}_4$ (Figs. 3f and S8). As seen in Fig. S8, when the anode is only undergoing OER, current densities of $10 \text{ mA}/\text{cm}^2$ and $100 \text{ mA}/\text{cm}^2$ require 1.28 V and 1.69 V, respectively. After the addition of 50 mM HMF, the current density of $10 \text{ mA}/\text{cm}^2$ and $100 \text{ mA}/\text{cm}^2$ is 60 mV (1.22 V) and 120 mV (1.57 V) lower than

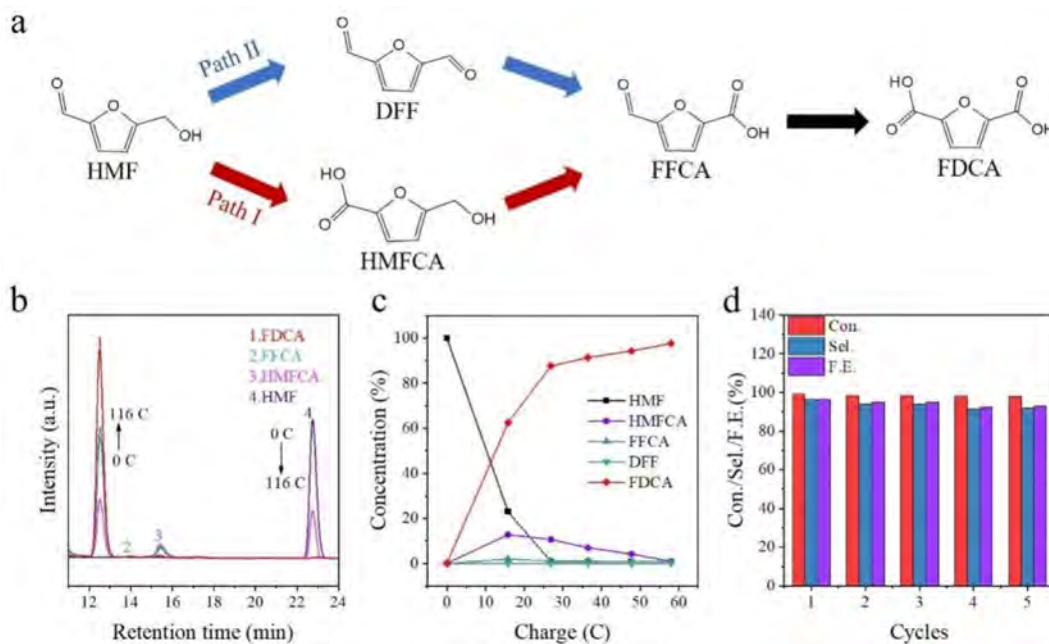


Fig. 4. (a) Two possible pathways of HMF oxidation to FDCA. (b) HPLC traces of HMF electro-oxidation catalyzed by $\text{Ni}_3\text{S}_2/\text{MoS}_2/\text{NiMoO}_4$ at 1.393 V vs. RHE in 10 mL 1.0 M KOH with 10 mM HMF. (c) Conversion changes of HMF during the HMFOR process. (d) The HMFOR of $\text{Ni}_3\text{S}_2/\text{MoS}_2/\text{NiMoO}_4$ under five successive cycles.

those of OER, respectively, indicating that HMFOR successfully replaced OER at the anode. Moreover, this performance is also significantly better than NiMoO_4 and Ni_3S_2 (Fig. 3f).

2.3. Chronoamperometry electrolysis measurements

Normally, there are two possible oxidation paths for HMF as shown in Fig. 4a; the corresponding intermediates are generated by oxidation of CHO or OH groups on the furan ring [25,26]. In path I, α -C on the aldehyde group desorbs H and recaptures OH^- in the solution to form a carboxyl group. On the contrary, in path II, the dehydrogenation site binds to H on the hydroxyl group, and α -C attaches itself to the hydroxyl group to form an aldehyde group after dehydrogenation. No matter which oxidation path occurs, HMF will be oxidized to 5-formyl-2-furancarboxylic acid (FFCA) intermediates and eventually to 2,5-furandicarboxylic acid (FDCA) [27]. Thus, to investigate the oxidative pathway of HMFOR on the $\text{Ni}_3\text{S}_2/\text{MoS}_2/\text{NiMoO}_4$, the chronoamperometric electrolysis measurements were performed on $\text{Ni}_3\text{S}_2/\text{MoS}_2/\text{NiMoO}_4$ by applying a 1.393 V vs. RHE in 10 mL electrolyte containing 1.0 M KOH and 10 mM HMF, and the oxidation intermediates and final product of HMF during electrolysis were detected using high-performance liquid chromatography. According to Fig. 4b, the theoretical charge required to fully convert HMF to FDCA is 116 C (the response time of different oxidation products of HMF in HPLC is shown in Fig. S9). This is because six electrons are necessary to electrooxidize one HMF molecule into FDCA. The electrooxidation of HMF takes place with the accumulation of charge transfer, which will ultimately lead to an increase in the final content of the FDCA in the product. The intermediate products, HMFCFA and FFCA, are consumed as part of this process, while the content of 2,5-diformylfuran (DFF) remains negligible. Simultaneously, the color of the anode electrolyte turns from dark red to transparent with oxidation times (Fig. S10), serving as further evidence of these findings. These outcomes indicate that HMF undergoes oxidation on the $\text{Ni}_3\text{S}_2/\text{MoS}_2/\text{NiMoO}_4$ catalyst through pathway I, from selective oxidation of the aldehyde group to a carboxyl group to form the intermediate HMFCFA, followed by the

oxidation of the hydroxyl group to FDCA. $\text{Ni}_3\text{S}_2/\text{MoS}_2/\text{NiMoO}_4$ exhibits superior catalytic performance, with a calculated HMF conversion rate, FDCA selectivity, and Faraday efficiency (FE) of FDCA for $\text{Ni}_3\text{S}_2/\text{MoS}_2/\text{NiMoO}_4$ at 99.2%, 96.7%, and 96.5%, respectively.

The cycling stability of the $\text{Ni}_3\text{S}_2/\text{MoS}_2/\text{NiMoO}_4$ electrode toward HMFOR was further evaluated with five cycles of HMFOR process via submerging the electrode in 10 mL of 1.0 M KOH solution containing 10 mM HMF. Once the previously introduced HMF was electrooxidized, a fresh 10 mM HMF was added to the electrolytic cell, as shown in Fig. S11. The narrow fluctuation amplitude of HMF conversion (98.0–99.1%), FDCA selectivity (92.1–96.7%), and FE of FDCA (96.4–92.7%) demonstrate good cyclic stability of the $\text{Ni}_3\text{S}_2/\text{MoS}_2/\text{NiMoO}_4$ electrode (Fig. 4d).

2.4. Mechanism of HMFOR and DFT calculations

To better understand the reaction mechanism of HMFOR on the $\text{Ni}_3\text{S}_2/\text{MoS}_2/\text{NiMoO}_4$ catalyst, the structural evolution of $\text{Ni}_3\text{S}_2/\text{MoS}_2/\text{NiMoO}_4$ and NiMoO_4 catalysts was monitored by in-situ Raman spectroscopy during OER and HMFOR reactions at different potentials (Figs. 5a–c and S12). At open circuit voltage (OCP), Raman peaks at 375 and 405 /cm for $\text{Ni}_3\text{S}_2/\text{MoS}_2/\text{NiMoO}_4$ catalysts are attributed to the A_{1g} mode and E^{1}_{2g} mode of the MoS_2 [18]. In addition, peaks at 709, 907, and 957/cm are attributed to the Ni–Mo–O bond and the Mo=O double bond, which are consistent with the Raman spectrum analysis in Fig. 2b [16,28]. When only OER proceeds on the electrode surface, the intensities of Mo–S, Ni–Mo–O, and Mo=O peaks gradually decreased with increasing voltage, indicating the decreased crystalline characteristics during the surface construction process. Additionally, new Raman peaks attributed to $\text{Ni}^{\text{III}}\text{—OOH}$ were detected at 466 and 542/cm when the voltage applied was increased to 1.45 V, which is consistent with the recorded LSV curve in Fig. 3a [29,30]. Then, after the introduction of HMFOR into the electrolyte, the characteristic peak of $\text{Ni}^{\text{III}}\text{—OOH}$ was still detectable at 1.45 V for the NiMoO_4 catalyst (Fig. 5b). Based on our previous research, the $\text{Ni}^{\text{III}}\text{—OOH}$ species present on the catalyst surface is the actual active species for the HMFOR [24]. This species undergoes a redox reaction

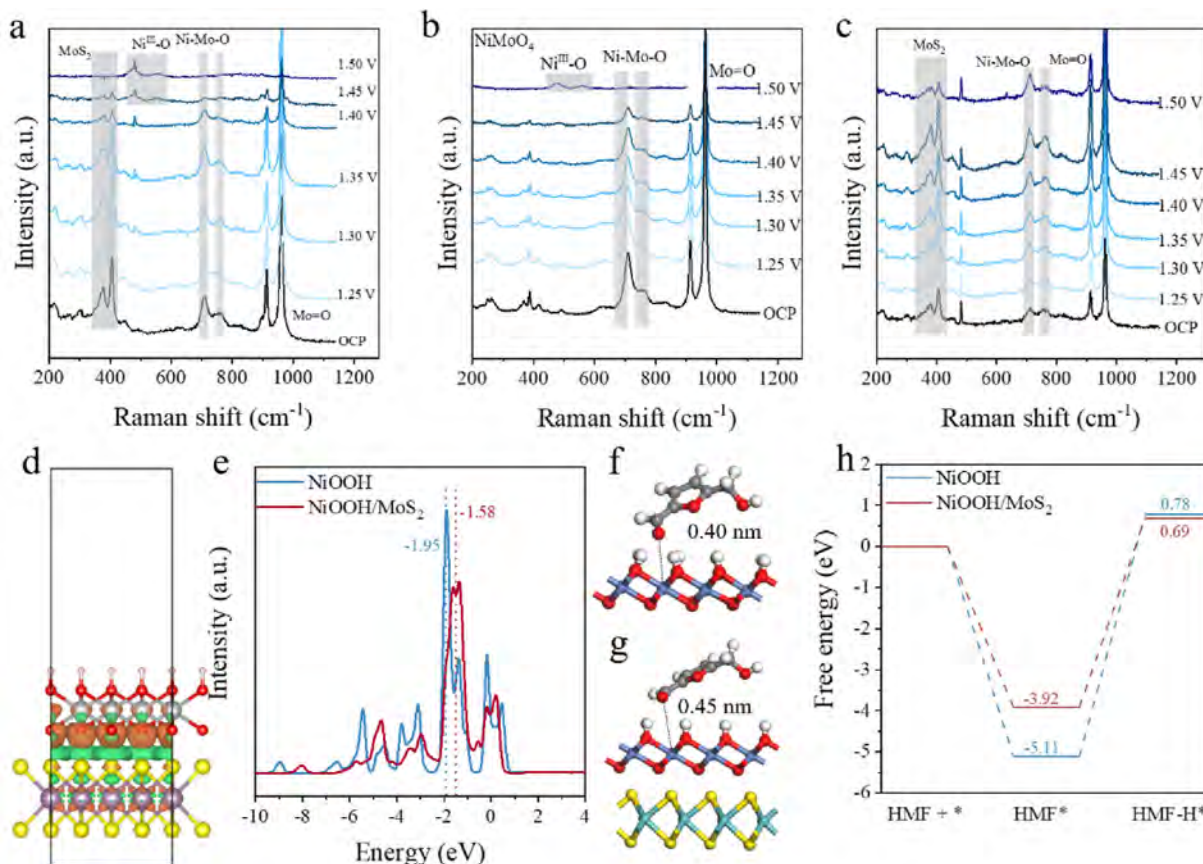


Fig. 5. (a) In-situ Raman spectra of $\text{Ni}_3\text{S}_2/\text{MoS}_2/\text{NiMoO}_4$ during OER (1.0 M KOH) under increasing potential from OCP to 1.50 V vs. RHE. (b) In-situ Raman spectra of NiMoO_4 during HMFOR (1.0 M KOH with 50 mM HMF). (c) In-situ Raman spectra of $\text{Ni}_3\text{S}_2/\text{MoS}_2/\text{NiMoO}_4$ during HMFOR. (d) The charge density difference in the heterostructure of MoS_2 and Ni_3S_2 (yellow: sulfur; red: oxygen; white: hydrogen; gray: nickel; purple: molybdenum). (e) PDOS of NiOOH , $\text{NiOOH}/\text{MoS}_2$, and the Fermi energy is set to 0 eV. (f) and (g) Side views of the HMF adsorption configurations on different models and the corresponding energy of adsorption. (h) The free energies of HMF adsorption on NiOOH and $\text{NiOOH}/\text{MoS}_2$. OCP stands for the open circuit voltage.

with HMF, oxidizing the HMF while simultaneously reducing itself to a low-valence Ni^{II} species, resulting in a dynamic equilibrium. While because of the competition between the four-electron-transfer OER and the six-electron-transfer HMFOR under a high potential environment, the proceed OER process significantly decreases the reaction kinetics of HMFOR, which leads to a break in the dynamic redox equilibrium between the $\text{Ni}^{\text{III}}\text{-OOH}$ active species and the HMF. Consequently, part of the $\text{Ni}^{\text{III}}\text{-OOH}$ species remains on the surface and does not participate in the HMF reaction. Interestingly, for the $\text{Ni}_3\text{S}_2/\text{MoS}_2/\text{NiMoO}_4$ electrocatalyst, the characteristic peak of $\text{Ni}^{\text{III}}\text{-OOH}$ is not observed when the applied voltage even increased to 1.5 V (Fig. 5c).

To investigate the active phase stabilization mechanism of $\text{Ni}_3\text{S}_2/\text{MoS}_2/\text{NiMoO}_4$ at high voltages and the role of MoS_2 , density functional theory (DFT) calculation is conducted. Since NiMoO_4 merely acts as a supporting framework for the 2D $\text{Ni}_3\text{S}_2/\text{MoS}_2$ active catalyst, the theory model took into account only a single layer of NiOOH layer covering the MoS_2 surface. The calculated differential charge densities based on the model exhibits that electron transfers are highly localized at the interface, in which the oxygen atom functions as electron acceptors and sulfur atom acts as electron donors (Fig. 5d). Moreover, the density of states of NiOOH and $\text{NiOOH}/\text{MoS}_2$ show a continuous peak at the Fermi energy level, thereby revealing their inherent half-metallic characters (Fig. 5e) [31]. Meanwhile, since the d-band center model can serve as a good descriptor of the adsorbate-metal interaction, the calculated d-band center of NiOOH and $\text{NiOOH}/\text{MoS}_2$, relative to the Fermi

level, is -1.95 and -1.58 eV, respectively. The results suggest a reduced contact energy barrier and an enhanced adsorption capacity of HMF in the $\text{NiOOH}/\text{MoS}_2$ heterostructure. The optimized adsorption model of HMF on the catalyst surface was presented to provide a clearer understanding of this process (Fig. 5f and g). The optimized structure reveals that the spacing between oxygen atoms in HMF and the active catalyst was 0.40 and 0.45 nm for NiOOH and $\text{NiOOH}/\text{MoS}_2$, indicating that smaller adsorption energies are necessary for HMF to create the stable adsorption state on the catalyst surface. Additionally, a more comprehensive analysis of the kinetic processes is shown in Fig. 5h. The free energies of HMF adsorption on NiOOH and $\text{NiOOH}/\text{MoS}_2$ were -5.11 and -3.92 eV, respectively. This obvious changed adsorption behavior demonstrates solid redox equilibrium can keep constant at a high voltage. Furthermore, the activation energy of the rate-determining step ($\text{HMF}^* \rightarrow \text{HMF-H}^*$) in $\text{NiOOH}/\text{MoS}_2$ is significantly lower than that of pure NiOOH , suggesting that the rapid mass and charge transfer kinetic guarantee the smooth progression of redox equilibrium reactions.

Importantly, the XRD and XPS results of the reacted samples are also provided to investigate the surface reconstruction process. As shown in Fig. S13, the relative intensity of Ni_3S_2 in the XRD pattern decreases, suggesting that some of the Ni_3S_2 is involved in surface reconstruction under the anodic voltage. Besides, the SEM and TEM images after HMFOR show that the morphology of $\text{Ni}_3\text{S}_2/\text{MoS}_2/\text{NiMoO}_4$ is almost unchanged (Figs. S14 and S15). Moreover, the XPS spectra of $\text{Ni}_3\text{S}_2/\text{MoS}_2/\text{NiMoO}_4$ after OER and HMFOR reactions are

shown in Figs. S16–18. In the Ni 2p spectrum, compared with the pristine Ni₃S₂/MoS₂/NiMoO₄ catalyst, the ratio of Ni³⁺/Ni²⁺ (average valence 2.67) increased to 2.84 after the OER process, and then average valence decreased to 2.17 after the HMFOR reaction, indicating the rapid accumulation of the Ni^{III}-OOH active species on the reconstructed NiOOH/MoS₂ surface (Fig. S16 and Table S2). However, when the HMFOR is carried out, since Ni^{III}-OOH is the real active site for the HMFOR, Ni^{III}-OOH is reduced to a low valence state, resulting in an increase in the average valence of Ni^{II} species [32]. This is in agreement with the in-situ Raman results. Moreover, in the Mo 3d spectrum, Mo⁴⁺ was oxidized to Mo⁶⁺ after either the OER or HMFOR reaction. In addition, two peaks located in 161.7 and 163.6 eV, which are attributed to S 2p_{3/2} and S 2p_{1/2}, respectively, can still be detected after HMFOR, indicating that Ni₃S₂/MoS₂/NiMoO₄ still maintains good structural stability after the reaction, and thus provides high catalytic performance (Figs. S17 and S18).

3. Conclusion

In conclusion, we designed and prepared Ni₃S₂/MoS₂/NiMoO₄ catalysts for the efficient and stable HMFOR. The nanosheet structure formed by the high-temperature treatment greatly increases the specific surface area of the catalyst and exposes more active sites. Combining theoretical calculations and experimental characterization, we demonstrate that the upward shift of the d-band center in the reconstructed NiOOH/MoS₂ facilitates the adsorption of HMF, which ensures a smooth redox equilibrium reaction at the high potential. As a result, the potential is reduced by 233 mV when the current density reaches 100 mA/cm² compared with that in the OER process. At the same time, the catalysts exhibit good performance for 5-hydroxymethylfurfural electrocatalytic oxidation reaction (HMFOR) in terms of selectivity (99.2%), conversion (96.7%), and Faraday efficiency (96.5%), and retain a stable Faraday efficiency after five cycles. Thus, our work provides new ideas for the synthesis of efficient and stable HMFOR catalysts for the sustainable green energy development.

4. Experimental section

4.1. Materials

Nickel nitrate hexahydrate (Ni(NO₃)₂·6H₂O), ammonium molybdate ((NH₄)₆Mo₇O₂₄·4H₂O), thiourea (CH₄N₂S), sulfur, potassium hydroxide (KOH), hydrochloric acid (HCl), ethanol (C₂H₆O), 5-hydroxymethylfurfural (HMF), 2,5-furandicarboxylic acid (FDCA), 2,5-diformylfuran (DFF), 5-formyl-2-furancarboxylic acid (FFCA), 2-furancarboxylic acid (HMFA), nickel foam (NF), deionized (DI) water was used throughout the experiment.

4.2. Preparation of NiMoO₄, Ni₃S₂, Ni₃S₂/MoS₂/NiMoO₄

Nickel foam (NF) was cut into small pieces measuring 1.0 × 3.0 cm². These small pieces were sonicated in an aqueous solution for 15 min in (3.0 M HCl), acetone, ethanol, and deionized water, respectively, then dried in an oven as the substrate. Typically, 0.3 mmol (NH₄)₆Mo₇O₂₄·4H₂O and 0.6 mmol Ni(NO₃)₂·6H₂O were mixed with 15 mL of deionized water. The mixture was then transferred to a stainless steel autoclave with a Teflon liner (25 mL). Then, a piece of 1.0 × 3.0 cm² NF was placed diagonally against the reactor. Afterward, the reactor was placed in an oven and heated to 150 °C and held for 6 h. At the end of the reaction, the autoclave reactor has been allowed to cool to room temperature by natural means. The NiMo precursor was taken out and washed with DI water thoroughly, and then it was dried inside a vacuum oven at 60 °C for 12 h. Finally,

the obtained NiMo precursor was placed downstream of the quartz tube, while the sulfur powder is placed upstream. After that, the oven has been heated up to 400 °C for 2 h in an Ar atmosphere, and then, the Ni₃S₂/MoS₂/NiMoO₄ electrocatalyst was obtained. The preparation of NiMoO₄ was similar to Ni₃S₂/MoS₂/NiMoO₄ except that it did not contain sulfur powder.

In addition, 0.75 mmol thiourea was dissolved in 15 mL DI water and then transferred to a 25 mL Teflon liner after stirring for 30 min. Then, a piece of 1.0 × 3.0/cm² NF was placed diagonally against the reactor. Therewith, we put the reactor into the oven at 140 °C and keep warm for 12 h. After the reaction, the autoclave reactor cooled to room temperature by natural means. The Ni₃S₂ was taken out and washed with DI water thoroughly, and then it was dried inside a vacuum oven at 50 °C for 10 h.

4.3. Physical characterizations

We determined the elemental composition of the samples by spherical aberration electron microscopy (Hitachi-HF 5000) and determined the distribution of each element over the catalyst. The phase diagrams of the prepared samples were derived by X-ray diffraction characterization in the 2θ range from 20° to 80° with a scan rate of 5°/min. The chemical composition and electronic structure of the samples were characterized by X-ray photoelectron spectroscopy. Raman spectroscopy (LabRAMHR 800 system) was performed at 532 nm laser on different samples.

4.4. Electrochemical methods

Room temperature was used for all electrochemical tests. The catalytic activity of the catalyst was tested by constructing a three-electrode test system using the prepared catalyst as the working electrode, platinum sheet as the counter electrode, and Ag/AgCl (1.0 M KCl) as the reference electrode. Test potentials are converted to standard hydrogen electrodes (RHE). Using linear sweep voltammetry (LSV) methods, the OER activities were measured at a scan rate of 5 mV/s in 1.0 M KOH electrolyte. LSV was also used to test the HMFOR activity of different catalysts, where the sweep speed was 5 mV/s and the polarization curves were corrected for iR compensation. In addition to this, the Tafel slope in the LSV polarization curve was calculated based on the Tafel equation [$\eta = b \cdot \log(j) + a$]. Then, the electrochemical impedance spectra were tested in the range of 100,000 Hz–0.01 Hz. The CV curves were tested in the potential range from 0.477 to 0.577 V vs. RHE at different scan rates (50–250 mV/s) as a means of comparing the double layer capacitance values (C_{dl}) of the different catalysts. The conversion tests of catalysts were evaluated by chronoamperometry at 1.393 V vs. RHE.

4.5. In-situ materials characterizations

In-situ Raman testing was done in a customized in-situ electrolysis cell. In-situ Raman spectroscopy was performed using different electrolytes (with and without HMF) with Ni₃S₂/MoS₂/NiMoO₄ and NiMoO₄ as working electrodes, Pt as the counter electrode, and Ag/AgCl (1.0 M KCl) as the reference electrode. Three Raman spectral signals were collected at each voltage at 70 s intervals. The voltage test was ranged from 1.25 to 1.50 V, where the voltage changes were modulated by an electrochemical workstation.

4.6. Alkaline anion exchange membrane water electrolyzer (AEMWE) test

The AEMWE system consists of an anode, a cathode, a gas diffusion layer and an anion exchange membrane (Fumasep, FAA-3-50). Ni₃S₂/MoS₂/NiMoO₄, NiMoO₄, and Ni₃S₂ were used as the

anode electrodes. Platinum modified NiFe LDH was used as the cathode electrode. When assembling the electrolyzer, it is ensure that each screw is installed with the same pressure. The catalytic activity of the three catalysts was evaluated by LSV at 1.0–2.0 V under ambient conditions with different electrolytes (with or without HMF) passed through the cell at a sweep rate of 5 mV/s.

4.7. Product quantification

The HPLC was equipped with a Xtimate Sugar-H 7.8 300 mm 5 μm chromatographic column for the electrooxidation of HMF, respectively. Final product identification and quantification are determined from calibration curves using commercially purchased standard solutions of known concentrations of pure starting materials, intermediates, and final products.

The alcohol–aldehyde conversion (%) and selectivity (%) of the oxidation products were calculated as follows:

$$\text{Alcohols} / \text{Aldehyde des conversion (\%)} = \frac{\text{mol of alcohols consumed}}{\text{mol of initial alcohols/aldehydes}} \times 100\%$$

$$\text{Product selectivity (\%)} = \frac{\text{mol of product formed}}{\text{mol of initial alcohols/aldehydes}} \times 100\%$$

The F.E. calculation formula:

$$\text{FE (\%)} = \frac{\text{mol of product formed}}{\text{total charged passed } \pm nF} \times 100\%$$

where F is the Faraday constant (96,485/mol) and n is the electron transfer number.

4.8. Theoretical calculations

Spin-polarized density functional theory calculations were carried out using the Vienna ab initio simulation package. We applied the projector-augmented wave potentials and Perdew–Burke–Ernzerhof (PBE) + U functional with a U–J value of 5.5 eV to investigate the d orbitals of nickel. The energy cutoff of 450 eV was used. The ionic relaxation loop would stop when the forces on all atoms were <0.02 eV/Å. HMF adsorption energy E_{ads} is defined as, $E_{\text{ads}}(\text{HMF}) = E_{\text{total}}(\text{HMF}/\text{surface}) - E_{\text{total}}(\text{surface}) - E_{\text{total}}(\text{HMF})$. $E_{\text{total}}(\text{HMF}/\text{surface})$, $E_{\text{total}}(\text{surface})$, and $E_{\text{total}}(\text{HMF})$ are the total energies of the optimized surface with adsorbed HMF, the optimized empty surface, and the optimized HMF molecule in the gas phase.

Credit author statement

Xiuming Bu: Conceptualization, Data curation, Formal analysis, Writing – review & editing. Yiwei Bao: Data curation, Formal analysis, Methodology, Writing – original draft. Yiqing Sun: Data curation, Formal analysis, Writing – original draft. Di Yin: Data curation, Formal analysis. Yuxuan Zhang: Resources, Software. Hao Zhang: Data curation, Formal analysis. Kaihang Yue: Data curation, Formal analysis. Xianying Wang: Funding acquisition, Project administration, Supervision, Writing – review & editing. Johnny Ho: Funding acquisition, Investigation, Project administration, Resources, Supervision, Writing – review & editing. Siwei Yang: Data curation, Formal analysis.

Declaration of competing interest

The authors declare that they have no known competing financial interests or personal relationships that could have appeared to influence the work reported in this paper.

Data availability

Data will be made available on request.

Acknowledgments

This work is financially supported by the Shanghai Sailing Program (23YF1455000) and the City University of Hong Kong (Project 7005650, 7020088 and 9229138).

Appendix A. Supplementary data

Supplementary data to this article can be found online at <https://doi.org/10.1016/j.mtener.2023.101463>.

References

- [1] E.B. Pomerantseva, Francesco Feng, Xinliang Cui, Yi. Y. Gogotsi, Energy storage: the future enabled by nanomaterials, *Science* 366 (2019) 6468–6480, <https://doi.org/10.1126/science.aan8285>.
- [2] Y. Meng, S. Yang, H. Li, Electro- and photocatalytic oxidative upgrading of bio-based 5-hydroxymethylfurfural, *ChemSusChem* 15 (2022) 2581–2596, <https://doi.org/10.1002/cssc.202102581>.
- [3] N. Kittner, F. Lill, D.M. Kammen, Energy storage deployment and innovation for the clean energy transition, *Nat. Energy* 2 (2017) 17125–17131, <https://doi.org/10.1038/nenergy.2017.125>.
- [4] P. Sudarsanam, R. Zhong, S. Van den Bosch, S.M. Coman, V.I. Parvulescu, B.F. Sels, Functionalised heterogeneous catalysts for sustainable biomass valorisation, *Chem. Soc. Rev.* 47 (2018) 8349–8402, <https://doi.org/10.1039/c8cs00410b>.
- [5] X. Wu, N. Luo, S. Xie, H. Zhang, Q. Zhang, F. Wang, Y. Wang, Photocatalytic transformations of lignocellulosic biomass into chemicals, *Chem. Soc. Rev.* 49 (2020) 6198–6223, <https://doi.org/10.1039/d0cs00314j>.
- [6] Y. Yang, T. Mu, Electrochemical oxidation of biomass derived 5-hydroxymethylfurfural (HMF): pathway, mechanism, catalysts and coupling reactions, *Green Chem.* 23 (2021) 4228–4254, <https://doi.org/10.1039/d1gc00914a>.
- [7] H. Zhang, J.H. Clark, T. Geng, H. Zhang, F. Cao, A carbon catalyst co-doped with P and N for efficient and selective oxidation of 5-hydroxymethylfurfural into 2,5-diformylfuran, *ChemSusChem* 14 (2021) 456–466, <https://doi.org/10.1002/cssc.202001525>.
- [8] A.H. Motagamwala, W. Won, C. Sener, D.M. Alonso, C.T. Maravelias, J.A. Dumesic, Toward biomass-derived renewable plastics: production of 2,5-furandicarboxylic acid from fructose, *Sci. Adv.* 4 (2018) 1–8, <https://doi.org/10.1126/sciadv.app9722>.
- [9] X. Huang, J. Song, M. Hua, Z. Xie, S. Liu, T. Wu, G. Yang, B. Han, Enhancing the electrocatalytic activity of CoO for the oxidation of 5-hydroxymethylfurfural by introducing oxygen vacancies, *Green Chem.* 22 (2020) 843–849, <https://doi.org/10.1039/c9gc03698a>.
- [10] Y. Xie, Z. Zhou, N. Yang, G. Zhao, An overall reaction integrated with highly selective oxidation of 5-hydroxymethylfurfural and efficient hydrogen evolution, *Adv. Funct. Mater.* 31 (2021) 2102886–2102897, <https://doi.org/10.1002/adfm.202102886>.
- [11] W. Chen, C. Xie, Y. Wang, Y. Zou, C.-L. Dong, Y.-C. Huang, Z. Xiao, Z. Wei, S. Du, C. Chen, B. Zhou, J. Ma, S. Wang, Activity origins and design principles of nickel-based catalysts for nucleophile electrooxidation, *Chem* 6 (2020) 2974–2993, <https://doi.org/10.1016/j.chempr.2020.07.022>.
- [12] M.T. Bender, Y.C. Lam, S. Hammes-Schiffer, K.-S. Choi, Unraveling two pathways for electrochemical alcohol and aldehyde oxidation on NiOOH,

- J. Am. Chem. Soc. 142 (2020) 21538–21547, <https://doi.org/10.1021/jacs.0c10924>.
- [13] N. Heidary, N. Kornienko, Electrochemical biomass valorization on gold-metal oxide nanoscale heterojunctions enables investigation of both catalyst and reaction dynamics with operando surface-enhanced Raman spectroscopy, *Chem. Sci.* 11 (2020) 1798–1806, <https://doi.org/10.1039/d0sc00136h>.
- [14] L. Zhou, S. Zeng, D. Zheng, Y. Zeng, F. Wang, W. Xu, J. Liu, X. Lu, NiMoO₄ nanowires supported on Ni/C nanosheets as high-performance cathode for stable aqueous rechargeable nickel-zinc battery, *Chem. Eng. J.* 400 (2020) 125832–125855, <https://doi.org/10.1016/j.cej.2020.125832>.
- [15] Y. Fan, X. He, H. Li, Y. Huang, C. Sun, H. Liu, E. Huangzhang, F. Sun, X. Zhao, J. Nan, Lithiophilic Ni₃S₂ layer decorated nickel foam (Ni₃S₂@Ni foam) with fast ion transfer kinetics for long-life lithium metal anodes, *Chem. Eng. J.* 450 (2022) 138384–138399, <https://doi.org/10.1016/j.cej.2022.138384>.
- [16] Z. Wang, J. Chen, E. Song, N. Wang, J. Dong, X. Zhang, P.M. Ajayan, W. Yao, C. Wang, J. Liu, J. Shen, M. Ye, Manipulation on active electronic states of metastable phase β-NiMoO₄ for large current density hydrogen evolution, *Nat. Commun.* 12 (2021) 5960–5970, <https://doi.org/10.1038/s41467-021-26256-1>.
- [17] Y.H.Y. Chen, K.H. Zhao, J.W. Cai, Z.Y. Wang, X. Y. Y. Yan, Effective modulating of the Mo dissolution and polymerization in Ni₄Mo/NiMoO₄ heterostructure via metal-metal oxide-support interaction for boosting H₂ production, *Chem. Eng. J.* 466 (2023) 143097–143107, <https://doi.org/10.1016/j.cej.2023.143097>.
- [18] T. Ren, W. Tian, Q. Shen, Z. Yuan, D. Chen, N. Li, J. Lu, Enhanced piezocatalysis of polymorphic few-layered MoS₂ nanosheets by phase engineering, *Nano Energy* 90 (2021) 106527–106538, <https://doi.org/10.1016/j.nanoen.2021.106527>.
- [19] S.A. Shah, R. Sayyar, L. Xu, H. Sun, I. Khan, J. Guo, X. Shen, S. Hussain, A. Yuan, H. Ullah, In-situ synthesis of NiS₂ nanoparticles/MoS₂ nanosheets hierarchical sphere anchored on reduced graphene oxide for enhanced electrocatalytic hydrogen evolution reaction, *J. Colloid Interface Sci.* 624 (2022) 150–159, <https://doi.org/10.1016/j.jcis.2022.05.112>.
- [20] B. Zhang, Z. Yang, C. Yan, Z. Xue, T. Mu, Operando forming of lattice vacancy defect in ultrathin crumpled NiVW-layered metal hydroxides nanosheets for valorization of biomass, *Small* 19 (2023), <https://doi.org/10.1002/smll.202207236>, 2207236–200746.
- [21] J. Zeng, W. Chen, G. Zhang, L. Yu, L. Zhong, Y. Liu, S. Zhao, Y. Qiu, Heterostructured Ni₃N-NiMoN nanowires as bifunctional electrocatalysts for hydrogen evolution and 5-hydroxymethylfurfural oxidation, *ACS Appl. Nano Mater.* 5 (2022) 7321–7330, <https://doi.org/10.1021/acsnm.2c01243>.
- [22] Y. Zhang, Z. Xue, X. Zhao, B. Zhang, T. Mu, Controllable and facile preparation of Co₉S₈-Ni₃S₂ heterostructures embedded with N,S,O-tri-doped carbon for electrocatalytic oxidation of 5-hydroxymethylfurfural, *Green Chem.* 24 (2022) 1721–1731, <https://doi.org/10.1039/d1gc04499k>.
- [23] B.J. Taitt, D.-H. Nam, K.-S. Choi, A comparative study of nickel, cobalt, and iron oxyhydroxide anodes for the electrochemical oxidation of 5-hydroxymethylfurfural to 2,5-furandicarboxylic acid, *ACS Catal.* 9 (2019) 660–670, <https://doi.org/10.1021/acscatal.8b04003>.
- [24] C.F.S. Liu, X.R. Yue, K.H. Wang, P.J. Zhan, K. Wang, X.Y. Xia, B. Y. Y. Yan, S-species-evoked high-valence Ni^{2+δ} of the evolved β-Ni(OH)₂ electrode for selective oxidation of 5-hydroxymethylfurfural, *Adv. Mater.* 35 (2023) 2211177–2211186, <https://doi.org/10.1002/adma.202211177>.
- [25] L. Zeng, Y. Chen, M. Sun, Q. Huang, K. Sun, J. Ma, J. Li, H. Tan, M. Li, Y. Pan, Y. Liu, M. Luo, B. Huang, S. Guo, Cooperative Rh-O₅/Ni(Fe) site for efficient biomass upgrading coupled with H₂ production, *J. Am. Chem. Soc.* 145 (2023) 17577–17587, <https://doi.org/10.1021/jacs.3c02570>.
- [26] Y. Lu, T. Liu, Y.-C. Huang, L. Zhou, Y. Li, W. Chen, L. Yang, B. Zhou, Y. Wu, Z. Kong, Z. Huang, Y. Li, C.-L. Dong, S. Wang, Y. Zou, Integrated catalytic sites for highly efficient electrochemical oxidation of the aldehyde and hydroxyl groups in 5-hydroxymethylfurfural, *ACS Catal.* 12 (2022) 4242–4251, <https://doi.org/10.1021/acscatal.2c00174>.
- [27] D.J. Chadderdon, L. Xin, J. Qi, Y. Qiu, P. Krishna, K.L. More, W. Li, Electrocatalytic oxidation of 5-hydroxymethylfurfural to 2,5-furandicarboxylic acid on supported Au and Pd bimetallic nanoparticles, *Green Chem.* 16 (2014) 3778–3786, <https://doi.org/10.1039/c4gc00401a>.
- [28] H.M. Abdel-Dayem, Dynamic phenomena during reduction of α-NiMoO₄ in different atmospheres: in-situ thermo-Raman spectroscopy study, *Ind. Eng. Chem. Res.* 46 (2007) 2466–2472, <https://doi.org/10.1021/ie0613476>.
- [29] W. Chen, Y. Wang, B. Wu, J. Shi, Y. Li, L. Xu, C. Xie, W. Zhou, Y.-C. Huang, T. Wang, S. Du, M. Song, D. Wang, C. Chen, J. Zheng, J. Liu, C.-L. Dong, Y. Zou, J. Chen, S. Wang, Activated Ni-OH bonds in a catalyst facilitates the nucleophile oxidation reaction, *Adv. Mater.* 34 (2022) 2105320–2105331, <https://doi.org/10.1002/adma.202105320>.
- [30] T. Wu, Z. Xu, X. Wang, M. Luo, Y. Xia, X. Zhang, J. Li, J. Liu, J. Wang, H.-L. Wang, F. Huang, Surface-confined self-reconstruction to sulfate-terminated ultrathin layers on NiMo₃S₄ toward biomass molecule electro-oxidation, *Appl. Catal. B Environ.* 323 (2023) 122126–122154, <https://doi.org/10.1016/j.apcatb.2022.122126>.
- [31] X. Liu, K. Ni, B. Wen, R. Guo, C. Niu, J. Meng, Q. Li, P. Wu, Y. Zhu, X. Wu, L. Mai, Deep reconstruction of nickel-based precatalysts for water oxidation catalysis, *ACS Energy Lett.* 4 (2019) 2585–2592, <https://doi.org/10.1021/acsenrgylett.9b01922>.
- [32] Y. Sun, J. Wang, Y. Qi, W. Li, C. Wang, Efficient electrooxidation of 5-hydroxymethylfurfural using co-doped Ni₃S₂ catalyst: promising for H₂ production under industrial-level current density, *Adv. Sci.* 9 (2022) 2200957–2200967, <https://doi.org/10.1002/advs.202200957>.